Available online at www.sciencedirect.com
ScienceDirect
Trans. Nonferrous Met. Soc. China 31(2021) 3063−3074
Transactions of Nonferrous Metals Society of China
www.tnmsc.cn

Microstructural and mechanical properties assessment of transient liquid phase bonding of CoCuFeMnNi high entropy alloy

Mohammad Ali KARIMI, Morteza SHAMANIAN, Mohammad Hossein ENAYATI

Department of Materials Engineering, Isfahan University of Technology, Isfahan 84156-83111, Iran

Received 4 November 2020; accepted 3 August 2021

Abstract: The transient liquid phase (TLP) bonding of CoCuFeMnNi high entropy alloy (HEA) was studied. The TLP bonding was performed using AWS BNi-2 interlayer at 1050 °C with the TLP bonding time of 20, 60, 180 and 240 min. The effect of bonding time on the joint microstructure was characterized by SEM and EDS. Microstructural results confirmed that complete isothermal solidification occurred approximately at 240 min of bonding time. For samples bonded at 20, 60 and 180 min, athermal solidification zone was formed in the bonding area which included Cr-rich boride and Mn_3Si intermetallic compound. For all samples, the γ solid solution was formed in the isothermal solidification zone of the bonding zone. To evaluate the effect of TLP bonding time on mechanical properties of joints, the shear strength and micro-hardness of joints were measured. The results indicated a decrement of micro-hardness in the bonding zone and an increment of micro-hardness in the adjacent zone of joints. The minimum and maximum values of shear strength were 100 and 180 MPa for joints with the bonding time of 20 and 240 min, respectively.

Key words: high entropy alloy; CoCuFeMnNi alloy; transient liquid phase bonding; bonding time; solid solution; isothermal solidification; microstructure; mechanical properties

1 Introduction

High entropy alloys (HEAs) are often defined as alloys which include five or more vital alloying elements with the concentration in the range of 5−35 at.% [1−4]. HEAs have received great attention due to their excellent properties such as high-temperature resistance, acceptable thermal durability, high-temperature strength, remarkable corrosion behavior, cryogenic ductility, suitable wear resistance, and good fatigue properties [5,6].

Successful welding of HEAs with no defect can broaden their application range [7,8]. There are a large number of studies on the fabrication and the properties of HEAs [9]. However, there are a few reports on the welding processes of HEAs in the literature. Consequently, it is critical to investigate the welding behavior of HEAs [10]. The welding of HEAs has been carried out by different methods such as electron beam welding (EBW), gas tungsten arc welding (GTAW), friction stir welding (FSW), laser beam welding (LBW) and spot welding [7,8,10−19]. For instance, JO et al [14] successfully applied FSW and LBW welding techniques for the joining of CoCrFeMnNi HEA. Chemical inhomogeneity between dendritic and interdendritic areas and a large fluctuation in chemical composition of fusion zone were observed in samples welded by LBW process. However, they reported that mechanical properties of joints were comparable to annealed base metal. The weldability of CoCrFeMnNi HEA was also investigated by WU et al [7]. It was reported that there were no welding defects in the heat affected and fusion zones. Furthermore, the weldments had appropriate mechanical properties due to significant amounts of twinning activity in the fusion zone [7]. GTAW of

Corresponding author: Morteza SHAMANIAN, Tel: +98-3133915737, E-mail: shamanian@cc.iut.ac.ir
DOI: 10.1016/S1003-6326(21)65715-1

a rolled CoCuFeMnNi HEA was recently carried out by OLIVEIRA et al [20]. CoCrFeMnNi HEA exhibited good weldability and no welding defects were witnessed in the joint area. However, large grain size and low hardness of the fusion zone resulted in a decrease in the fracture strain of the joints [20].

CoCuFeMnNi HEA, with a similar amount of cobalt, copper, iron, manganese, and nickel, has been investigated [9,21,22]. It has been reported that CoCuFeMnNi HEA has single-phase face center cubic (FCC) structure [9,21−23]. In addition, this alloy exhibits appropriate tensile strength, ductility, and hardness [9,21]. The promising excellent mechanical properties make the CoCuFeMnNi HEA a potential candidate for engineering applications. In addition, it is crystal clear that welding process is one of the most important stages of developing new materials for engineering applications. In fact, welding allows the fabrication of intricately shaped structures from simple components [20]. Therefore, the influence of bonding process on new CoCuFeMnNi HEA needs to be studied before it can be developed for an engineering application. Hence, in this study an attempt was made to investigate the effect of bonding process on the microstructure and mechanical properties of CoCuFeMnNi HEA.

Transient liquid phase (TLP) bonding is an alternative welding method for joining of advanced materials [24]. The TLP bonding process was carried out using an interlayer which contains melting point depressant (MPD) [25,26] or eutectic phase forming with constituent elements of base metals [27,28]. In interlayers with MPD elements, the diffusion of elements from interlayer to base metals and vice versa takes place. The diffusion of MPD elements leads to the increment of the interlayer's melting point and the solidification of melted interlayer occurs at constant temperature [29]. The TLP bonding includes the advantages of diffusion bonding and brazing [30,31]. The presence of the interlayer in the TLP bonding process leads to formation of a thin liquid film between parent metals which removes the limitations of the diffusion bonding such as high surface smoothness and high bonding pressure [32−34]. Bonding at a temperature lower than the melting point of base metal [35] and the absence of bonding distortion in the base metal are among other advantages of the TLP bonding process [28,30]. Therefore, TLP bonding process could be an appropriate method for joining of CoCuFeMnNi HEA.

Thus far, there are no studies on the TLP bonding process of HEAs. In the present work, we intended to characterize the microstructure and mechanical properties of CoCuFeMnNi HEA welded by TLP bonding using AWS BNi-2 interlayer with focus on TLP bonding time.

2 Experimental

2.1 Materials

The base metal samples with the dimensions of 12 mm × 10 mm × 3 mm were prepared by wire cutting of spark plasma sintered CoCuFeMnNi HEA. AWS BNi-2 amorphous alloy with 50 μm in thickness and dimensions of 12 mm × 10 mm was utilized as the interlayer. The chemical compositions of the base metal and AWS BNi-2 interlayer are given in Table 1.

Table 1 Chemical compositions of base metal and AWS BNi-2 interlayer (at.%)

Material	Co	Cu	Fe	Mn	Ni	Cr	Si	B	C
Base metal	21.3	18.1	21.4	18.2	21	−	−	−	
AWS BNi-2	−	−	3	−	Bal.	7	4.5	3.2	0.06

2.2 Preparation of samples

The preparation of the samples was carried out by grinding on 180 to 2400 grit SiC papers. Then, samples and interlayer were cleaned by acetone in an ultrasonic bath for 20 min and were dried at room temperature. The AWS BNi-2 interlayer was subsequently laid between HEA samples. The TLP bonding was performed using a vacuum furnace with the vacuum of 665×10^{-5} Pa at 1050 °C for 20, 60, 180 and 240 min. The selected bonding temperature was 50 °C higher than the melting point of AWS BNi-2 interlayer (1000 °C).

2.3 Microstructure characterization

The TLP bonded and base metal samples were cut and their cross-sections were ground by 800 to 2400 grit SiC papers and polished with 1 and 0.05 μm of alumina powder. Field emission scanning electron microscope (FESEM, Quanta 450−FEG-FEI) and scanning electron microscope

(SEM, Philips XL30) were used to characterize the microstructure of base metal and TLP bonded samples. Investigation of the concentration profiles of alloying elements and the chemical composition of phases formed at the bonding zone of joints were carried out using energy dispersive spectroscopy (EDS). Phase identification of base metal and fracture surfaces was carried out using X-ray diffractometry in a Philips X'Pert-MPD system with Cu K_α radiation at 2θ=10°−90°.

2.4 Mechanical properties measurement

Hardness profile across the cross-section of samples was determined using the Vickers micro-hardness tester (Micromet-S101, Mitutoyo, Japan) under the load of 100 g and dwell time of 10 s. In order to investigate the shear strength of the TLP joints, three samples of each bonding condition were tested at the loading rate of 0.5 mm/min based on the AWS C3.2M/C3.2 standard. The schematic of the fixture used for the shear test is presented in Fig. 1. Fracture surfaces of samples after shear tests were analyzed using SEM and XRD.

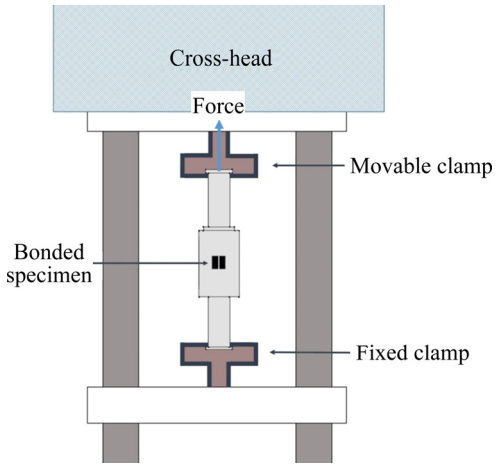

Fig. 1 Schematic of shear strength fixture

3 Results and discussion

3.1 Assessment of base metal microstructure

CoCuFeMnNi HEA base metal was fabricated through spark plasma sintering technique. The FESEM images of base metal are shown in Fig. 2. The microstructure of base metal consists of a single-phase solid solution. The dark areas on the image are residual pores. As can be seen in Fig. 2, the porosity level in balk sample is very low. The porosity level, measured by Archimedes method, was about 3%.

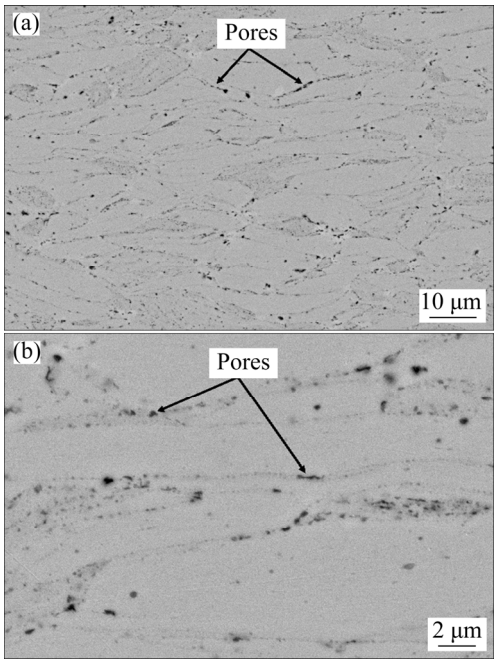

Fig. 2 Microstructure of CoCuFeMnNi HEA base metal fabricated by spark plasma sintering at low (a) and high (b) magnifications

3.2 Microstructure of joints

SEM micrographs of TLP joints generated at 1050 °C for 20, 60, 180, and 240 min are shown in Fig. 3. There are different distinguished areas in the bonding zone (BZ) of all the samples: base metal (BM), isothermal solidification zone (ISZ), and athermal solidification zone (ASZ).

In comparison to the microstructure of initial base metal (Fig. 2), the porosity level of base metal has not changed after the TLP bonding process. Fine dark spots observed in base metal microstructure are pores which were formed during the TLP bonding process due to thermal cycles of joining procedure. As can be seen, the irregularly shaped pores of base metal have changed into spherical and larger pores after bonding process.

In order to investigate the phase transformation of CoCuFeMnNi HEA, XRD patterns of base metal before and after the bonding process at 1050 °C with different holding time are presented in Fig. 4. It is observed that no new phases were formed in base metal during the TLP bonding process.

The formation of the intermetallic compounds in the joint area of Figs. 3(a−c) revealed that bonding time was not sufficient. Therefore, the isothermal solidification was not complete and as a

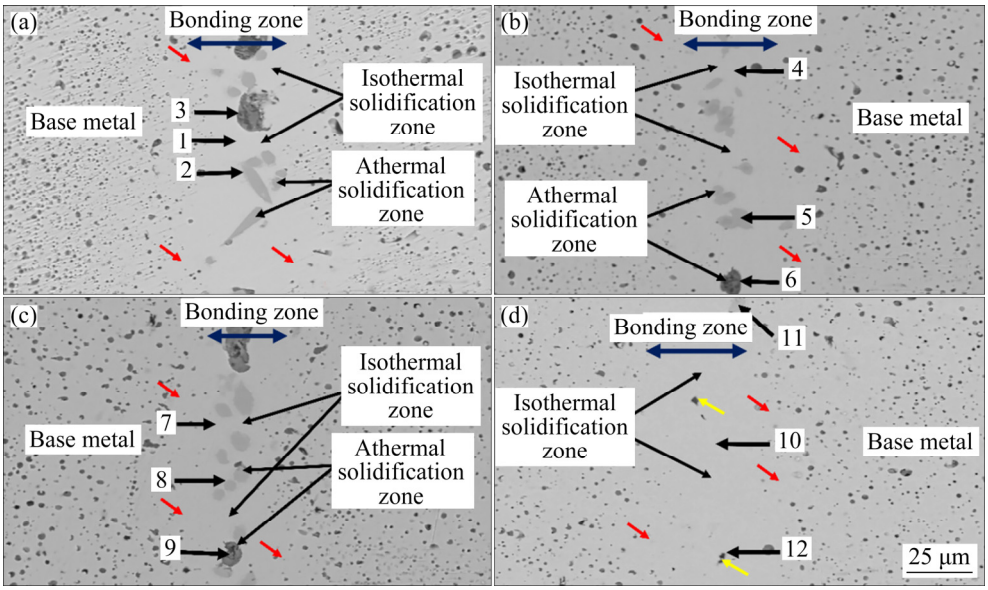

Fig. 3 SEM images of TLP bonded samples fabricated at 1050 °C for 20 min (a), 60 min (b), 180 min (c), and 240 min (d)

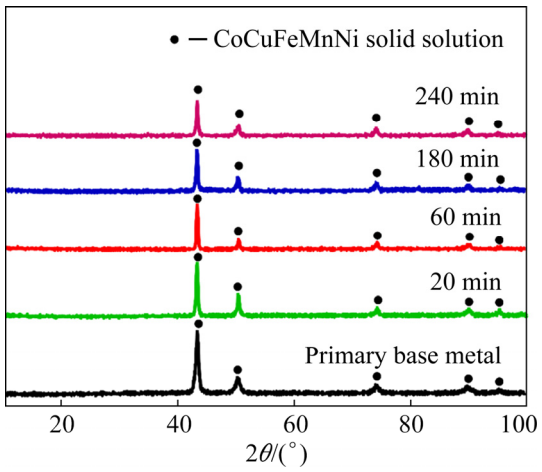

Fig. 4 XRD patterns of base metal before and after TLP bonding process at 1050 °C with bonding time of 20 min, 60 min, 180 min, and 240 min

result, ASZ was formed at joints with TLP bonding time of 20, 60 and 180 min. In fact, insufficient bonding time leads to the formation of ASZ and intermetallic compounds [36−38]. Thus, the microstructures of samples with the bonding time of 20, 60 and 180 min are identical. In order to achieve a uniform free intermetallic compounds microstructure, the bonding time was increased up to 240 min. The microstructure of TLP bonded sample produced at 1050 °C for 240 min (Fig. 3(d)) indicated that increasing TLP bonding time up to 240 min resulted in an almost perfect isothermal solidification due to the elimination of the most of intermetallic compounds. As seen in Fig. 3(d), only a few traces of the intermetallic compounds are observed which were shown by yellow arrows.

The thickness of the bonding zone was calculated using ImageJ image analysis software (Table 2). It can be seen that the width of the joint areas decreased compared to the thickness of the AWS BNi-2 initial interlayer (50 μm). The decrement in the joints' width can be ascribed to the diffusion of elements from interlayer. Consequently, it can be suggested that diffusion affected zone (DAZ) was formed next to the bonding zone, but DAZ cannot be clearly observed on the microstructure due to pores of base metals. Nevertheless, the microstructure of base metals around the bonding zone (red arrows) is slightly different from far ones. In these regions, the density of pores is lower than that in other regions.

Table 2 Width of joint regions at different bonding time

Bonding time/min	Joints width/μm
20	42
60	34
180	30
240	42

Bonding time of 20 min was insufficient for the diffusion of B, Cr, Si and Ni atoms to adjacent HEA. Thus, the thickness of the joint area was similar to the initial interlayer thickness (about 42 μm). Increasing the bonding time up to 180 min

reduced the width of the bonding areas to 30 μm.

As it can be perceived from Fig. 3(d), the bonded region of the joint with 240 min bonding time is greater than other samples. In fact, increasing the bonding time to 240 min leads to almost complete isothermal solidification, dissolution of base metals and diffusion of elements from base metals to the bonded area. According to the Fick's laws, the concentration gradient of constituent elements resulted in the migration of these components from base to the centerline of joint [39].

EDS analysis results of different regions of TLP joints marked in Fig. 3 are presented in Table 3. Different phases formed in the TLP bonding zone (Spots 1−9) are elaborated as follows. EDS analysis results of Spots 1, 4, 7, and 10, which are located in ISZ, suggest that γ solid solution was formed. Formation of the γ solid solution was also reported in previous works on TLP bonding using nickel-based interlayers [36−40]. The absence of Ni-silicide was due to relatively good solubility of Si in γ solid solution [36]. It could be seen that the amount of Co, Cu, Fe, and Mn increased with respect to the chemical composition of the initial interlayer (Table 1) due to the dissolution of base metal and diffusion of elements from base metals to bonding region. Furthermore, comparison of EDS analysis results for isothermal solidification zone of different samples (Spots 1, 4, 7, and 10) shows that increase in bonding time increases the concentration of main components of base metal (Co, Cu, Fe, and Mn elements) while the concentration of main component of AWS BNi-2 interlayer (Ni element) in the bonding zone reduces. This could be related to higher diffusion of elements as the bonding time increases from 20 to 240 min.

Gray phases (Spots 2, 5, 8, and 11) in the bonding zone are probably Cr-rich borides. Formation of γ solid solution during the TLP bonding process and cooling from bonding temperature leads to rejection of B and Cr elements into the residual melt. Therefore Cr-rich and Ni-rich borides might be formed [36]. Cr-rich borides were also observed in several works which utilized AWS BNi-2 as an interlayer [41−44]. The fraction of intermetallic compounds was noticeable for samples bonded for 20, 60 and 180 min. According to the microstructure of joints, it can be seen that most of the Cr-rich borides are eliminated when the bonding time increased to 240 min due to the diffusion of constituent elements of MPD from interlayer to adjacent base metals. For sample with the bonding time of 240 min, there have been sufficient time for diffusion of B and Si elements from interlayer into the adjacent base metal.

The time needed to complete isothermal solidification depends on the solid-state diffusion of MPD atoms from interlayer to base metal [45,46]. GHASEMI et al [45] used the Fick's law and provided the following equation for the flux (J) of MPD atoms from the interlayer to the base metal:

Table 3 EDS results of different areas marked in Fig. 3 (at.%)

Spot	Co	Cu	Fe	Mn	Ni	Cr	Si	Deduced phase
1	6.9	8.6	9.7	10.3	50.5	3.1	10.9	γ solid solution
2	0.9	0.7	1.6	3	1.4	89.9	2.5	Cr-rich boride
3	0.4	0.5	0.3	52.2	0.6	0.7	45.3	Mn-silicide
4	7.5	8.7	11.5	13.9	44.6	3	10.8	γ solid solution
5	5.1	0.7	12.3	5.2	4.8	67.6	4.3	Cr-rich boride
6	0.5	0.7	0.3	42.4	0.7	0.7	54.7	Mn-silicide
7	10.5	12.2	13.9	16.7	37.4	2.2	7.1	γ solid solution
8	6.2	0.5	13	8.9	4.7	63.7	3	Cr-rich boride
9	0.9	0.7	1.5	51.9	1.5	0.8	42.7	Mn-silicide
10	10.7	13.4	14.6	17.5	36.4	0.5	6.9	γ solid solution
11	7.1	0.4	16.5	13.6	3.1	56.7	2.6	Cr-rich boride
12	0.9	0.4	2.9	50.4	2	0.1	43.3	Mn-silicide

$$J=\frac{\sqrt{D_s}\ (C_s-C_{bm})}{\sqrt{\pi t}} \quad (1)$$

where C_{bm} is the initial composition of MPD in the base metal, C_s is the equilibrium concentration of MPD in solid phase (base metal) at the solid/liquid interface, and D_s is the diffusion coefficient for MPD atoms. According to this equation, two key factors control the flux of atoms during the TLP process which include the follows [45].

(1) Diffusion kinetics: MPD atoms with higher diffusion coefficients result in higher atomic flux and therefore shorter isothermal solidification time. Diffusion coefficient is a function of the intrinsic characteristics of MPD and base metal atoms. It is therefore necessary to investigate the diffusion coefficient of MPD atoms of the AWS B-Ni2 interlayer into the base material. In general, diffusion rate of interstitial atoms (such as boron atoms in AWS BNi-2 interlayer) is higher than that of substitutional atoms (such as silicon atoms in AWS BNi-2 interlayer) [45]. However, reports also indicate that the diffusion rate is lower in high entropy alloys which is known as the sluggish diffusion effect [47−51]. Therefore, it is predicted that MPD atoms will have low diffusivity in the base metal.

(2) Diffusion thermodynamics: The difference between the concentration of MPD atoms in the interlayer/base metal interface (C_s) and the concentration of MPD atoms in the base metal (C_{bm}) is the driving force of the diffusion. Higher difference in concentration of MPD atoms between interface and base metal results in higher thermodynamic driving force for diffusion of MPD atoms and reduces the time necessary for isothermal solidification [45]. In bonding of CoCuFeMnNi HEA using AWS BNi-2 interlayer, C_{bm}=0. Therefore, the solid solubility of MPD in the base metal (C_s) will be the determining factor in thermodynamic driving force for diffusion. Therefore, the higher solubility of MPD atoms in the solid phase interface will result in faster isothermal solidification. Evaluation of binary phase diagrams for base metal components (Co, Cu, Fe, Mn and Ni) with MPD atoms present in the interlayer (B and Si atoms) indicates that MPD atoms have low solubility in the components of the base metal which in turn reduces the solubility of MPD atoms in this alloy. Therefore, the thermodynamic driving force of diffusion is low when AWS BNi-2 interlayer is used for the TLP bonding of CoCuFeMnNi alloy.

Based on these facts, it appears that the reasons for longer isothermal solidification time are the sluggish diffusion effect in high entropy alloys and low solubility of MPD atoms in the CoCuFeMnNi HEA base metal.

EDS analysis results of dark phases (Spots 3, 6, 9, and 12) in the microstructure of TLP bonded samples revealed that Mn-silicide compound is formed in the joint zone. XRD pattern for fracture surface of sample bonded at 20 min shows the existence of Mn_3Si in the bonded area.

As can be seen from the microstructure of joints, the amount of silicides is smaller than borides because the solubility of Si element in base metal is higher than the B element. In addition, the diffusion coefficient of B element is higher than that of the Si element due to the smaller atomic radius. At constant temperature, smaller atomic radius results in lower diffusion activation energy and therefore larger diffusion coefficient. Furthermore, the diffusion mechanism of B element is interstitial and the diffusion mechanism of Si element is substitutional. In the interstitial diffusion, the diffusion of atoms is relatively simple since the atoms diffuse in the empty interatomic spaces. However, in the substitutional diffusion, atoms can only diffuse to a neighboring vacancy. This can result in different activation energies between interstitial and substitutional diffusion mechanisms. The activation energy for interstitial diffusion (Q_{ID}) is equal to the changes in migration enthalpy (ΔH_m) while activation energy of substitutional diffusion (Q_{SD}) includes migration enthalpy (ΔH_m) as well as the formation enthalpy for 1 mol of vacancies (ΔH_v). In other words,

$$Q_{ID}=\Delta H_m \quad (2)$$

$$Q_{SD}=\Delta H_m+\Delta H_v \quad (3)$$

This means that the requirement for the presence of vacancy in substitutional diffusion results in higher activation energy and lower diffusion coefficient. It has also been reported that the fraction of silicides in the bonding zone of TLP bonded samples is lower than borides [52]. As it was expected, increasing the TLP bonding time led to almost complete removal of Mn_3Si phase from the bonding zone.

The variation of element concentration across the bonding zone for samples with the bonding time of 20 and 240 min are shown in Fig. 5. The presence of constituent elements of the base metal in the bonding zone indicates that the dissolution of base metal occurs during TLP bonding process. As can be seen from Fig. 5, at longer TLP bonding time, the concentration profile smoothed due to sufficient time for diffusion of elements from base metal into interlayer and vice versa. Formation of Cr-rich and silicide phases in joint with the TLP bonding time of 20 min is associated with the fluctuation in Ni concentration.

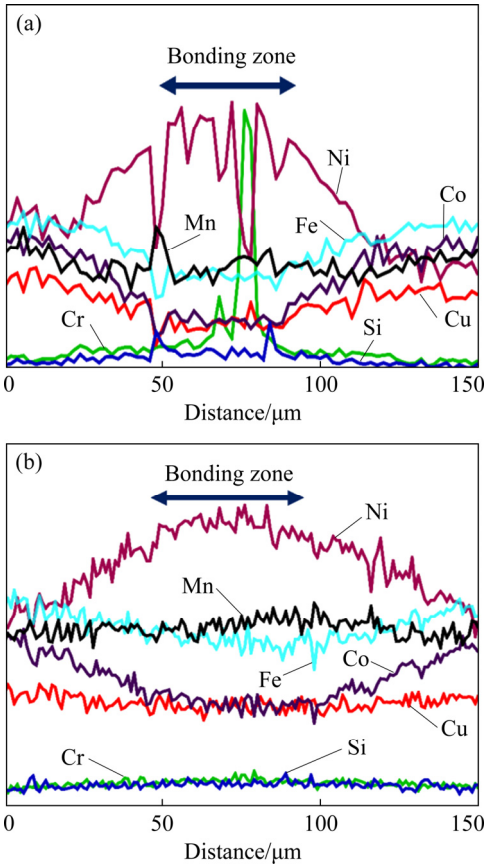

Fig. 5 EDS line analysis of TLP bonded samples bonded at 1050 °C for 20 min (a) and 240 min (b)

Considerable chemical composition fluctuations in the welding zone of HEAs welded by fusion welding processes have been reported in others researches [14,53]. These fluctuations in chemical composition can affect the mechanical properties of the welded specimens. Hence, chemical composition homogeneity in the bonding zone of TLP bonded sample with the bonding time of 240 min is a key advantage in comparison with other welding techniques.

3.3 Shear strength evaluation

To assess the effect of the bonding time at 1050 °C on the shear strength, samples with different TLP bonding time of 20, 60, 180, and 240 min were evaluated by shear strength test, and the results are presented in Fig. 6. As can be seen, the shear strength of TLP bonded samples improves with increasing the bonding time. Shear strength changes can be attributed to the formation of intermetallic compounds in the bonding zone. Low shear strength for 20 and 60 min is related to the high amount of Cr-rich borides and Mn_3Si intermetallic compound. The difference between the shear strength of these samples can be ascribed to the morphology of phases formed in the bonding zone. As it could be seen from Fig. 3(a), some of the Cr-rich borides in isothermal solidification zone (ISZ) showed needle-shaped morphology which led to the lower shear strength of the sample with the bonding time of 20 min. As a matter of fact, needle-shaped phases facilitated the crack propagation in the bonding zone. Reduction in athermal solidification zone (ASZ) phases for the sample with the holding time of 180 min led to higher shear strength of the joint with the bonding time of 180 min. By raising the TLP bonding time to 240 min and achieving an approximately fully isothermal solidification, the shear strength of joint increased due to the elimination of ASZ phases. Similar results were also reported previously [54,55]. The maximum shear strength of joints (180 MPa) was about 50% of shear strength of the base metal (320 MPa).

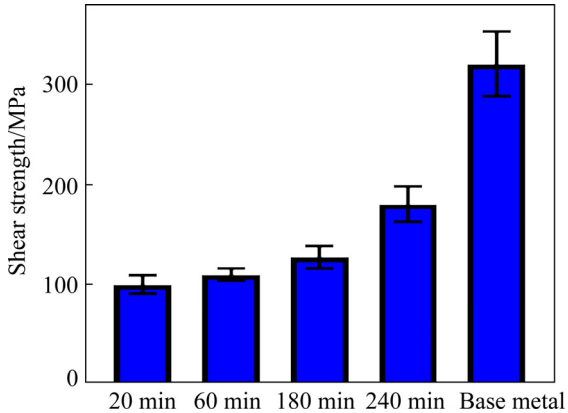

Fig. 6 Variations of shear strength of TLP bonded samples at various TLP bonding time

3.4 Micro-hardness

In order to appraise the effect of TLP bonding

time on micro-hardness of TLP bonded joints, the Vickers hardness of different samples was measured. The average value of hardness for initial base metal was 330 $HV_{0.1N}$. As it was explained in Section 3.2, after TLP bonding process, the porosity shape and the porosity size of base metal changed, leading to a drop in the hardness value of base metal. The maximum hardness value of base metal after TLP bonding was 273 $HV_{0.1N}$ which is significantly lower than that of initial base metal. As can be seen in Fig. 7, the hardness value of the base metal for all samples showed noticeable fluctuations. These results are attributed to the porous microstructure of base metals.

Typically, by increasing the TLP bonding time, the heat input induced by bonding process increases. Therefore, as can be seen from Fig. 7, the average hardness of base metal decreased. The decrement in the micro-hardness value of the bonded area in different samples is related to γ solid solution formation and isothermal solidification. Furthermore, it can be seen that with increasing the bonding time from 20 to 240 min, the micro-hardness value of the bonded area increases. This could be related to the concentration increment of base metal constituent elements (Co, Cu, Fe, and Mn elements) in the bonding zone which is reported in Table 3 and discussed in Section 3.2.

Regarding the hardness value in the adjacent zone of joints, it could be observed that the hardness value increased in adjacent base metal. The increment hardness value in the adjacent base metal could be due to the formation of hard compounds in DAZ. Similar results were also reported by AMIRI et al [54] in TLP joints of GTD-111/Ni−Cr−Fe−B−Si/GTD111system.

3.5 Fracture surfaces analysis

Fracture surface images of samples prepared at 1050 °C with different TLP bonding time are illustrated in Fig. 8. As it was anticipated from the microstructure of joints, the brittle fracture took place in the joints with the bonding time of 20, 60 and 180 min due to the presence of the intermetallic

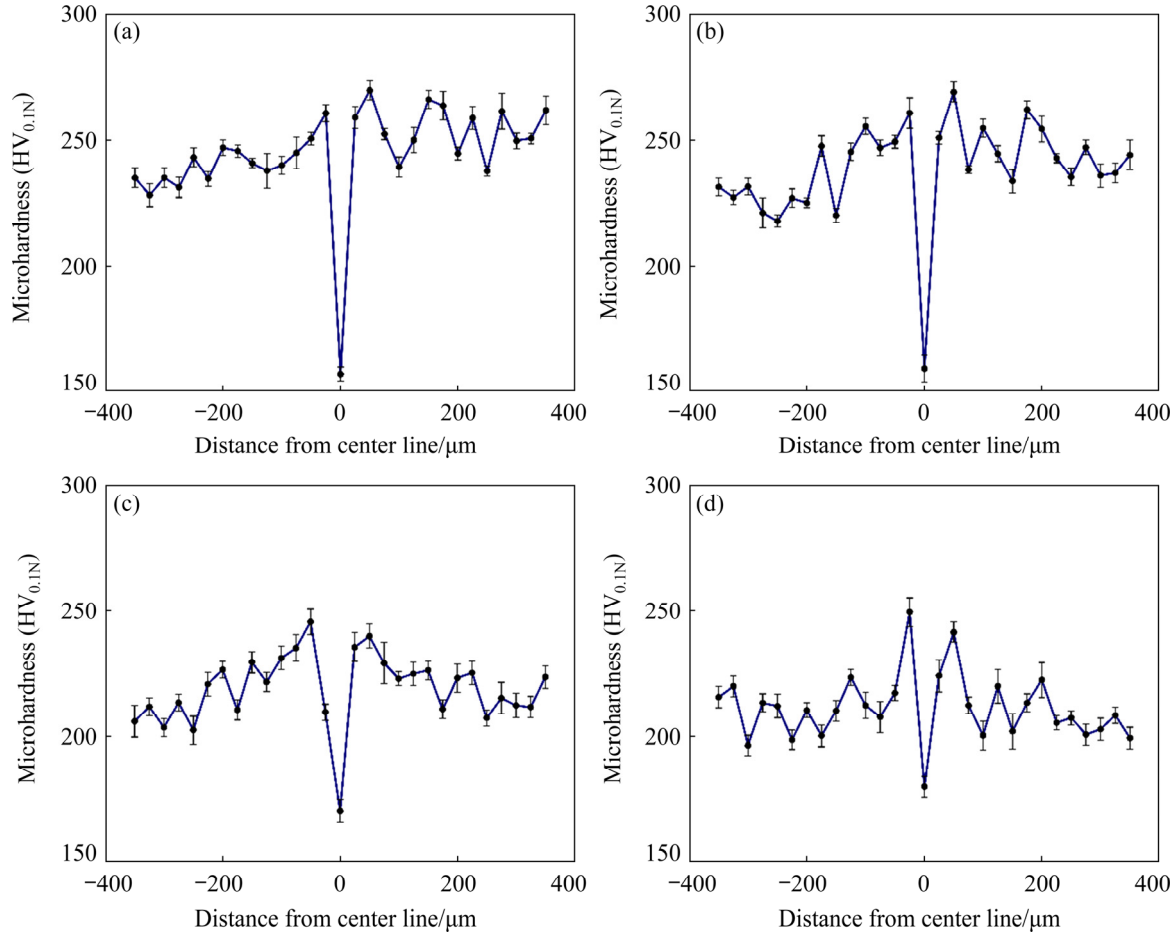

Fig. 7 Micro-hardness profiles of TLP joints bonded at 1050 °C for different bonding time: (a) 20 min; (b) 60 min; (c) 180 min; (d) 240 min

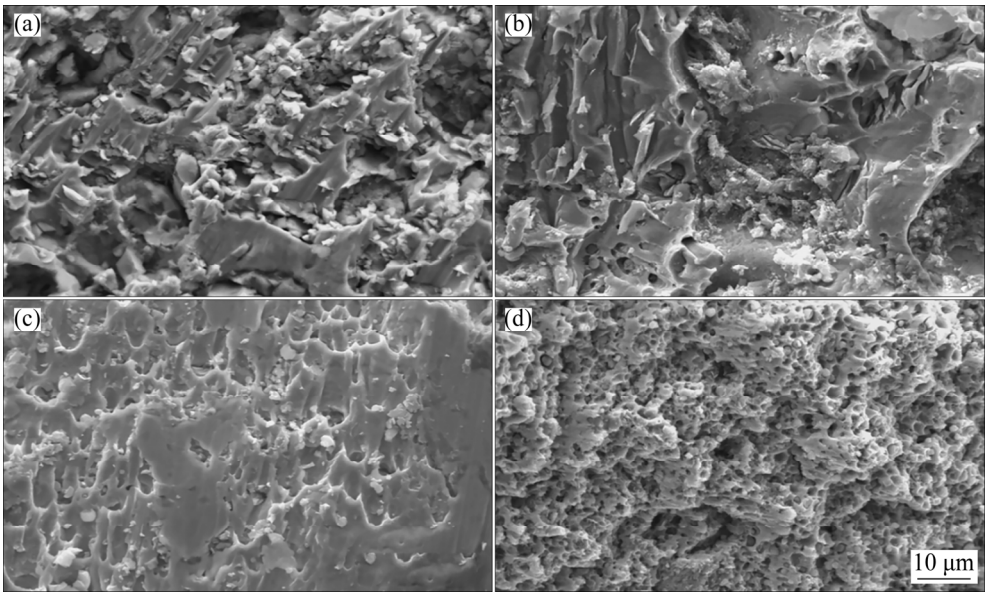

Fig. 8 SEM images of fracture surfaces of TLP joints bonded at 1050 °C for 20 min (a), 60 min (b), 180 min (c), and 240 min (d)

compounds in the joint area which facilitated crack propagation. Cleavage planes on fracture surface are indicant of brittle fracture (see Figs. 8(a−c)). These observations justify the low shear strength of these samples. Figure 8(d) illustrates the fracture surface of TLP bonded joint with the holding time of 240 min. The domination of dimples on the fracture surface showed that ductile fracture occurred in this situation. These results are in agreement with the microstructure and mechanical properties of TLP bonded joints reported earlier [36].

The XRD patterns of fracture surfaces for joints generated with the bonding time of 20 and 240 min are presented in Fig. 9. As can be seen from Fig. 9, Cr_2B, and Mn_3Si phases were formed in the sample with the bonding time of 20 min. The XRD pattern of the fracture surface of the sample with the holding time of 240 min showed only peaks pertaining to CoCuFeMnNi HEA base metal with no intermetallic compounds observed in fracture surface.

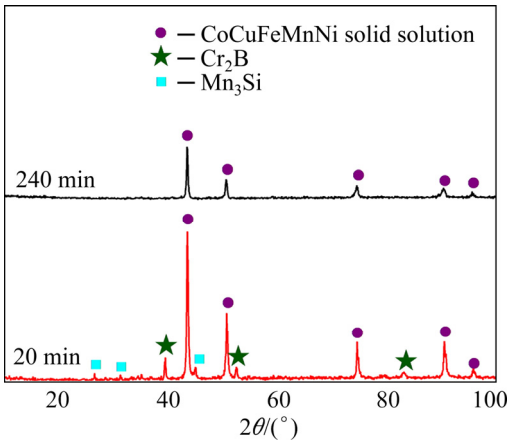

Fig. 9 XRD patterns of fracture surfaces for samples with bonding time of 20 min and 240 min

4 Conclusions

(1) The microstructural investigations of TLP bonded joints showed that by increasing the holding time up to 240 min, the complete isothermal solidification was almost achieved in the joint region.

(2) The γ solid solution was formed in ISZ of the bonding zone for all samples. Intermetallic compounds including Cr-rich borides and Mn_3Si were formed in ASZ of samples with the bonding time of 20, 60, and 180 min.

(3) The results indicated decrement of micro-hardness value in the bonding zone and the increment micro-hardness value in the adjacent zone of joints.

(4) The maximum shear strength of 180 MPa and the ductile fracture mechanism were achieved in the sample with the bonding time of 240 min as a result of the isothermal solidification. The joint with the bonding time of 20 min exhibited the lowest

shear strength due to the presence of a considerable amount of intermetallic compounds with a needle-shaped morphology.

References

[1] REN Ming-xing, LI Bang-sheng, FU Heng-zhi. Formation condition of solid solution type high-entropy alloy [J]. Transactions of Nonferrous Metals Society of China, 2013, 23: 991−995.

[2] WU S W, XU L, MA X D, JIA Y F, MU Y K, JIA Y D, WANG G, LIU C T. Effect of annealing temperatures on microstructure and deformation behavior of Al0.1CrFeCoNi high-entropy alloy [J]. Materials Science and Engineering A, 2021, 805: 140523.

[3] ZHOU Shang-cheng, ZHANG Peng, XUE Yun-fei, WANG Fu-chi, LU Wang, CAO Tang-qing, ZHEN Tan, CHENG Bao-yuan, WANG Ben-peng. Microstructure evolution of Al0. 6CoCrFeNi high entropy alloy powder prepared by high pressure gas atomization [J]. Transactions of Nonferrous Metals Society of China, 2018, 28: 939−945.

[4] LI Bao-yu, KUN PENG, HU Ai-ping, ZHOU Ling-ping, ZHU Jia-jun, LI De-yi. Structure and properties of FeCoNiCrCu0.5Alx high-entropy alloy [J]. Transactions of Nonferrous Metals Society of China, 2013, 23: 735−741.

[5] SAAL J E, BERGLUND I S, SEBASTIAN J T, LIAW P K, OLSON G B. Equilibrium high entropy alloy phase stability from experiments and thermodynamic modeling [J]. Scripta Materialia, 2018, 146: 5−8.

[6] SUN S J, TIAN Y Z, LIN H R, YANG H J, DONG X G, WANG Y H, ZHANG Z F. Transition of twinning behavior in CoCrFeMnNi high entropy alloy with grain refinement [J]. Materials Science and Engineering A, 2018, 712: 603−607.

[7] WU Z G, DAVID S A, FENG Z L, BEI H B. Weldability of a high entropy CrMnFeCoNi alloy [J]. Scripta Materialia, 2016, 124: 81−85.

[8] WU Z G, DAVID S A, LEONARD D N, FENG Z L, BEI H B. Microstructures and mechanical properties of a welded CoCrFeMnNi high- entropy alloy [J]. Science and Technology of Welding and Joining, 2018, 23: 585−595.

[9] BISWAS K, GURAO N P. Deciphering micro-mechanisms of plastic deformation in a novel single phase fcc-based MnFeCoNiCu high entropy alloy using crystallographic texture [J]. Materials Science and Engineering A, 2016, 657: 224−233.

[10] ZHU Z G, SUN Y F, GOH M H, NG F L, NGUYEN Q B, FUJII H, NAI S M L, WEI J, SHEK C H. Friction stir welding of a CoCrFeNiAl0.3 high entropy alloy [J]. Materials Letters, 2017, 205: 142−144.

[11] ZHEREBTSOV S, STEPANOV N, SHAYSULTANOV D, MALOPHEYEV S, VYSOTSKIY I, SANIN V, KASHAEV N, KAIBYSHEV R. Use of novel welding technologies for high-entropy alloys joining [C]//Materials Science Forum. Trans Tech Publ, 2018: 919−924.

[12] ZHU Z G, NG F L, QIAO J W, LIAW P K, CHEN H C, NAI S M L, WEI J, BI G J. Interplay between microstructure and deformation behavior of a laser-welded CoCrFeNi high entropy alloy [J]. Materials Research Express, 2019, 6: 046514.

[13] SOKKALINGAM R, SIVAPRASAD K, MUTHUPANDI V, DURAISELVAM M. Characterization of laser beam welded Al0.5CoCrFeNi high-entropy alloy [C]//Key Engineering Materials. Trans Tech Publ, 2018: 448−453.

[14] JO M G, KIM H J, KANG M J, MADAKASHIRA P P, PARK E S, SUH J Y, KIM D I, HONG S T, HAN H N. Microstructure and mechanical properties of friction stir welded and laser welded high entropy alloy CrMnFeCoNi [J]. Metals and Materials International, 2018, 24: 73−83.

[15] CUI Lang, MA Bing, FENG Sheng-qiang, WANG Xiu-ling. Microstructure and mechanical properties of high-entropy alloys CoCrFeNiAl by welding [C]//Advanced Materials Research. Trans Tech Publ, 2014: 1635−1640.

[16] KASHAEV N, VENTZKE V, STEPANOV N, SHAYSULTANOV D, SANIN V, ZHEREBTSOV S. Laser beam welding of a CoCrFeNiMn-type high entropy alloy produced by self-propagating high-temperature synthesis [J]. Intermetallics, 2018, 96: 63−71.

[17] NAM H, PARK C, KIM C, KIM H, KANG N. Effect of post weld heat treatment on weldability of high entropy alloy welds [J]. Science and Technology of Welding and Joining, 2018, 23: 420−427.

[18] SHAYSULTANOV D, STEPANOV N, MALOPHEYEV S, VYSOTSKIY I, SANIN V, MIRONOV S, KAIBYSHEV R, SALISHCHEV G, ZHEREBTSOV S. Friction stir welding of a carbon-doped CoCrFeNiMn high-entropy alloy [J]. Materials Characterization, 2018, 145: 353−361.

[19] SOKKALINGAM R, MISHRA S, CHEETHIRALA S R, MUTHUPANDI V, SIVAPRASAD K. Enhanced relative slip distance in gas-tungsten-arc-welded $Al_{0.5}$CoCrFeNi high-entropy alloy [J]. Metallurgical and Materials Transactions A, 2017, 48: 3630−3634.

[20] OLIVEIRA J P, CURADO T M, ZENG Z, LOPES J G, ROSSINYOL E, PARK J M, SCHELL N, FERNANDES F M B, KIM H S. Gas tungsten arc welding of as-rolled CrMnFeCoNi high entropy alloy [J]. Materials & Design, 2020, 189: 108505.

[21] SONKUSARE R, KHANDELWAL N, GHOSH P, BISWAS K, GURAO N P. A comparative study on the evolution of microstructure and hardness during monotonic and cyclic high pressure torsion of CoCuFeMnNi high entropy alloy [J]. Journal of Materials Research, 2019, 34: 732−743.

[22] SONKUSARE R, JANANI P D, GURAO N P, SARKAR S, SEN S, PRADEEP K G, BISWAS K. Phase equilibria in equiatomic CoCuFeMnNi high entropy alloy [J]. Materials Chemistry and Physics, 2018, 210: 269−278.

[23] GURAO N P, BISWAS K. In the quest of single phase multi-component multiprincipal high entropy alloys [J]. Journal of Alloys and Compounds, 2017, 697: 434−442.

[24] NOROUZI E, ATAPOUR M, SHAMANIAN M, ALLAFCHIAN A. Effect of bonding temperature on the microstructure and mechanical properties of Ti−6Al−4V to AISI 304 transient liquid phase bonded joint [J]. Materials & Design, 2016, 99: 543−551.

[25] KWON Y S, KIM J S, MOON J S, SUK M J. Transient liquid phase bonding process using liquid phase sintered alloy as an interlayer material [J]. Journal of Materials Science, 2000, 35: 1917−1924.

[26] MALEKI V, OMIDVAR H, RAHIMIPOUR M R. Effect of gap size on microstructure of transient liquid phase bonded IN-738LC superalloy [J]. Transactions of Nonferrous Metals Society of China, 2016, 26: 437−447.

[27] MAITY J, PAL T K, MAITI R. Transient liquid phase diffusion bonding of 6061-13vol.%SiC_p composite using Cu powder interlayer: Mechanism and interface characterization [J]. Journal of Materials Science, 2010, 45: 3575−3587.

[28] COOK GRANT O, SORENSEN CARL D. Overview of transient liquid phase and partial transient liquid phase bonding [J]. Journal of Materials Science, 2011, 46: 5305−5323.

[29] KHAZAEI B A, ASGHARI G, BAKHTIARI R. TLP bonding of dissimilar FSX-414/IN738 system with MBF80 interlayer: Prediction of solid/liquid interface location [J]. Transactions of Nonferrous Metals Society of China, 2014, 24: 996−1003.

[30] NOROUZI E, SHAMANIAN M, ATAPOUR M, KHOSRAVI B. Diffusion brazing of Ti−6Al−4V and AISI 304: an EBSD study and mechanical properties [J]. Journal of Materials Science, 2017, 52: 12467−12475.

[31] MALEKI V, OMIDVAR H, RAHIMIPOUR M R. Influences of gap size and cyclic-thermal-shock treatment on mechanical properties of TLP bonded IN-738LC superalloy [J]. Transactions of Nonferrous Metals Society of China, 2018, 28: 920−930.

[32] WU Xiao-wei, CHANDEL R S, LI Hang. Evaluation of transient liquid phase bonding between nickel-based superalloys [J]. Journal of Materials Science, 2001, 36: 1539−1546.

[33] ILLINGWORTH T C, GOLOSNOY I O, GERGELY V, CLYNE T W. Numerical modelling of transient liquid phase bonding and other diffusion controlled phase changes [J]. Journal of Materials Science, 2005, 40: 2505−2511.

[34] ABDOLVAND R, ATAPOUR M, SHAMANIAN M, ALLAFCHIAN A. The effect of bonding time on the microstructure and mechanical properties of transient liquid phase bonding between SAF 2507 and AISI 304 [J]. Journal of Manufacturing Processes, 2017, 25: 172−180.

[35] JAMALOEI A D, KHORRAM A, JAFARI A. Characterization of microstructure and mechanical properties of dissimilar TLP bonding between IN718/IN600 with BNi-2 interlayer [J]. Journal of Manufacturing Processes, 2017, 29: 447−457.

[36] GHONEIM A, OJO O A. Microstructure and mechanical response of transient liquid phase joint in Haynes 282 superalloy [J]. Materials Characterization, 2011, 62: 1−7.

[37] NOROUZI E, ATAPOUR M, SHAMANIAN M. Effect of bonding time on the joint properties of transient liquid phase bonding between Ti−6Al−4V and AISI 304 [J]. Journal of Alloys and Compounds, 2017, 701: 335−341.

[38] POURANVARI M, EKRAMI A, KOKABI A H. Microstructure development during transient liquid phase bonding of GTD-111 nickel-based superalloy [J]. Journal of Alloys and Compounds, 2008, 461: 641−647.

[39] ESMAEILI H, MIRSALEHI S E, FARZADI A. Vacuum TLP bonding of Inconel 617 superalloy using Ni−Cr−Si−Fe−B filler metal: Metallurgical structure and mechanical properties [J]. Vacuum, 2018, 152: 305−311.

[40] MALEKAN A, FARVIZI M, MIRSALEHI S E, SAITO N, NAKASHIMA K. Influence of bonding time on the transient liquid phase bonding behavior of Hastelloy X using Ni−Cr−B−Si−Fe filler alloy [J]. Materials Science and Engineering A, 2019, 755: 37−49.

[41] HE Hong-jie, SHENG Guang-min, LIU Ming-can, JIAO Ying-jun. Microstructure and mechanical properties of transient liquid phase bonded joints of CB2 ferritic heat resistant steels with amorphous BNi-2 interlayer [J]. Rare Metal Materials and Engineering, 2018, 47: 2290−2297.

[42] ARAFIN M A, MEDRAJ M, TURNER D P, BOCHER P. Effect of alloying elements on the isothermal solidification during TLP bonding of SS 410 and SS 321 using a BNi-2 interlayer [J]. Materials Chemistry and Physics, 2007, 106: 109−119.

[43] KHORRAM A, FAKHRAEI O, TORKAMANY M J. Laser brazing of Inconel 718 and Inconel 600 with BNi-2 nickel-based filler metal [J]. The International Journal of Advanced Manufacturing Technology, 2017, 88: 2075−2084.

[44] JALILVAND V, OMIDVAR H, RAHIMIPOUR M R, SHAKERI H R. Influence of bonding variables on transient liquid phase bonding behavior of nickel based superalloy IN-738LC [J]. Materials and Design, 2013, 52: 36−46.

[45] GHASEMI A, POURANVARI M. Fast isothermal solidification during transient liquid phase bonding of a nickel alloy using pure copper filler metal: Solubility vs diffusivity [J]. Metallurgical and Materials Transactions A, 2019, 50: 2235−2245.

[46] OJO O A, RICHARDS N L, CHARTURVEDI M C. Effect of gap size and process parameters on diffusion brazing of Inconel 738 [J]. Science and Technology of Welding and Joining, 2004, 9: 209−220.

[47] WANG Gang, YANG Yun-long, HE Ru-jie, TAN Cai-wang, HUTTULA M, CAO Wei. A novel high entropy CoFeCrNiCu alloy filler to braze SiC ceramics [J]. Journal of the European Ceramic Society, 2020, 40: 3391−3398.

[48] WANG Gang, YANG Yun-long, WANG Miao, HE Ru-jie, TAN Cai-wang, CAO Wei, XU Hai-feng. Brazing ZrB_2-SiC ceramics to Nb with a novel CoFeNiCrCu high entropy alloy [J]. Journal of the European Ceramic Society, 2021, 41: 54−61.

[49] SHABANI A, TOROGHINEJAD M R. Evaluation of microstructure and texture formation during annealing of cold-rolled FeCrCuMnNi multiphase high-entropy alloy [J]. Transactions of Nonferrous Metals Society of China, 2020, 30: 449−462.

[50] CHENG Hu, XIE Yan-chong, TANG Qun-hua, RAO Cong, DAI Pin-qiang. Microstructure and mechanical properties of FeCoCrNiMn high-entropy alloy produced by mechanical alloying and vacuum hot pressing sintering [J]. Transactions of Nonferrous Metals Society of China, 2018, 28: 1360−1367.

[51] FU Jian-xin, CAO Cheng-ming, TONG Wei, PENG Liang-ming. Effect of thermomechanical processing on microstructure and mechanical properties of CoCrFeNiMn high entropy alloy [J]. Transactions of Nonferrous Metals Society of China, 2018, 28: 931−938.

[52] POURANVARI M, EKRAMI A, KOKABI A H. Solidification and solid state phenomena during TLP

bonding of IN718 superalloy using Ni−Si−B ternary filler alloy [J]. Journal of Alloys and Compounds, 2013, 563: 143−149.

[53] SOKKALINGAM R, VEERAPPAN M, SIVAPRASAD K, PRASHANTH K G. Dissimilar welding of Al0.1CoCrFeNi high-entropy alloy and AISI304 stainless steel [J]. Journal of Materials Research, 2019, 34: 1−12.

[54] AMIRI D, SAJJADI S A, BAKHTIARI R, KAMYABI-GOL A. The role of TLP process variables in improvement of microstructure and mechanical properties in TLP joints of GTD-111/Ni−Cr−Fe−B−Si/GTD-111 system [J]. Journal of Manufacturing Processes, 2018, 32: 644−655.

[55] HADIBEYK S, BEIDOKHTI BEHROOZ, SAJJADI SEYED ABDOLKARIM. Effect of bonding time and homogenization heat treatment on the microstructure and mechanical properties of the transient liquid phase bonded dissimilar GTD-111/FSX-414 TLP superalloys [J]. Journal of Alloys and Compounds, 2018, 731: 929−935.

CoCuFeMnNi 高熵合金瞬态液相连接的显微组织与力学性能评价

Mohammad Ali KARIMI, Morteza SHAMANIAN, Mohammad Hossein ENAYATI

Department of Materials Engineering, Isfahan University of Technology, Isfahan 84156-83111, Iran

摘　要：研究 CoCuFeMnNi 高熵合金(HEA)的瞬时液相(TLP)连接。TLP 连接使用 AWS BNi-2 夹层，温度为 1050 °C，时间分别为 20、60、180、和 240 min。采用扫描电镜和能谱仪表征连接时间对接头显微组织的影响。显微组织结果证实，约 240 min 时发生完全等温凝固。而连接时间为 20、60 和 180 min 的样品其连接区形成非热凝固区，含有富铬硼化物和 Mn_3Si 金属间化合物。所有样品接头的等温凝固区中均形成 γ-Ni 固溶体。为了研究 TLP 连接时间对接头力学性能的影响，测量接头的剪切强度和显微硬度。结果表明，接头显微硬度值较小，相邻区显微硬度值较大。连接时间为 20 min 的样品接头具有最低的剪切强度 100 MPa，而连接时间为 240 min 的样品具有最大的剪切强度 180 MPa。

关键词：高熵合金；CoCuFeMnNi 合金；瞬时液相连接；连接时间；固溶体；等温凝固；显微组织；力学性能

(Edited by Xiang-qun LI)